Aalborg Universitet

AALBORG UNIVERSITY

Magnetic Integration for Parallel Interleaved VSCs Connected in a Whiffletree Configuration

Gohil, Ghanshyamsinh Vijaysinh; Bede, Lorand; Teodorescu, Remus; Kerekes, Tamas; Blaabjerg, Frede

Magnetic Integration for Parallel Interleaved VSCs Connected in a Whiffletree Configuration

Ghanshyamsinh Gohil, *Student Member, IEEE,* Lorand Bede, *Student Member, IEEE,* Remus Teodorescu, *Fellow, IEEE,* Tamas Kerekes, *Member, IEEE,* and Frede Blaabjerg, *Fellow, IEEE,*

Abstract—The Voltage Source Converters (VSCs) are often connected in parallel to realize a high current rating. In such systems, the harmonic quality of the output voltage can be improved by interleaving the carrier signals of the parallel VSCs. However, an additional inductive filter is often required to suppress the circulating current that flows between the parallel interleaved VSCs. One of the ways to deal with the circulating current problem is to use the coupled inductors in a whiffletree configuration. This paper proposes the integration of the line filter inductor and the circulating current filter inductor in a single magnetic component for such systems. The fundamental frequency component of the flux is mostly confined to the limbs around which the coils are placed, whereas other parts of the magnetic structure only experiences high frequency flux excitation. As a result, the integrated inductor can be made smaller and the power density of the overall converter system can be increased. The magnetic structure of the integrated inductor is analyzed and performance is verified by simulation and experimental studies.

I. INTRODUCTION

In many high power applications, the two-level Voltage Source Converters (VSCs) are normally connected in parallel to meet the high current requirement and often share the common dc-link, as shown in Fig. 1. The Silicon Insulated Gate Bipolar Transistors (IGBTs) are normally used in high power applications and they suffer from excessive losses if the switching frequency is increased beyond a few kHz. Due to the this limitation, large passive filter components are generally employed to comply with the stringent power quality requirements. This lead to the increased cost, size and losses. Therefore the efforts are being made to reduce the size of these components. For a given switching frequency, one of the ways to reduce the filtering requirement is to employ a multi-level VSC.

For the parallel connected two-level VSCs, multi-level voltage waveforms can be achieved by interleaving the carrier signals. As a result of the interleaved carriers, some of the harmonic frequency components present in the switched output voltage of the parallel interleaved legs are phase shifted with respect to each other [1]–[7]. For the parallel connected VSCs, the output voltage of a given phase is the average of the switched output voltages of all parallel VSC legs of that phase. As a result of the averaging, the contribution of the phase shifted harmonic frequency components of the individual switched output voltages is fully or partially canceled in the resultant voltage [8], which leads to the reduction in the value of the filter components [9].
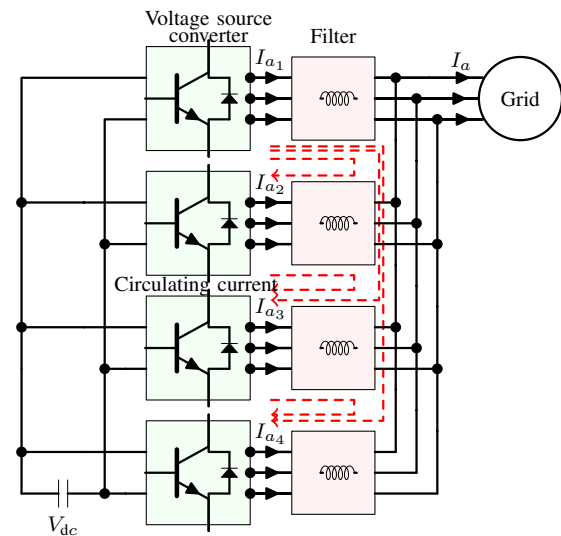
When connected to a common dc-link, the circulating

Fig. 1. Parallel voltage source converters with a common dc-link and output filters.

current flows between the parallel VSCs due to the hardware and control asymmetries [10], as shown in Fig. 1, where four VSCs are connected in parallel and shares the same dc-link. Five-level resultant voltage waveforms for each of the phases can be achieved by interleaving the carrier signals of these four parallel VSCs. However, the interleaving of the carrier signals further aggravates the already existing problem of the circulating current [7]. This unwanted circulating current increases the losses in both the semiconductor devices and in the passive components and it should be suppressed. An additional inductive filter is often required for this purpose. One of the solutions is to use a Coupled Inductor (CI). The CI can be designed to provide magnetic coupling between the parallel interleaved legs of the corresponding phases [1], [11]–[16]. By choosing a proper value of the magnetic coupling coefficient, desired value of the inductance can be offered to the circulating current component. In the case of the four parallel VSCs, the CIs are often connected in a whiffletree configurations, as proposed in [1] and reproduced in Fig. 2(b). Such arrangement requires two distinct inductive component:

1) Line filter inductor (L_f) for improving the injected line current quality.
2) CIs for suppressing the circulating current.

Although the interleaved carrier signals leads to the reduction in the value of the line filter inductor L_f, additional filter
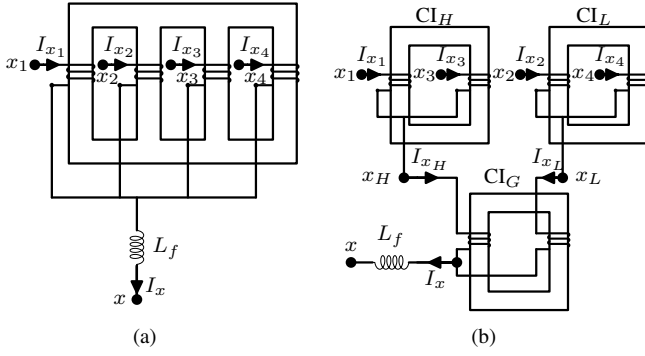
Fig. 2. Various arrangements of the filters for four parallel interleaved VSCs. (a) CI with four limb core structure, (b) Whiffletree configuration using the two limb CIs. The subscript x represents phases $x = \{a, b, c\}$.

Fig. 3. Whiffletree configuration for parallel interleaved voltage source converters [1].

components (CIs) are often required, as shown in Fig. 2(b). The volume of these inductive components can be reduced by integrating both of these functionalities into a single magnetic component. This paper proposes the magnetic integration of the line filter inductor L_f and the circulating current filters (which mainly experiences the switching frequency flux excitation) for a four parallel interleaved VSCs. The VSCs are divided into two converter groups and the carrier signals of the VSCs within each group are shifted by $180°$. In addition, the carrier signals of the VSCs of both the converter groups are also phase-shifted with respect to each other. Therefore, the circulating current flows between the VSCs of each of the converter group as well as between the two converter groups. The proposed integrated inductor offers desired line filter inductance L_f and also suppresses the circulating current between the VSCs within each of the converter groups. The circulating current between the converter groups is suppressed using an additional CI (referred to as a CI_G).

The paper is organized as follow: The issue of the circulating current and the overview of the existing filtering solutions are briefly discussed in Section II. The proposed integrated inductor is analyzed in Section III. The design equations of the coupled inductor that are used for circulating current suppression between the two converter groups are discussed in Section IV. The volume reduction achieved by the proposed solution is demonstrated in Section V, by comparing its volume with that of the state-of-the-art solution. The functionality of the integrated inductor is verified by performing simulation and experimental studies and the results are presented in Section VI.

II. CIRCULATING CURRENT IN A PARALLEL INTERLEAVED VSCs

The switched output voltages of the parallel legs are phase shifted with respect to each other due to the interleaved carriers. When VSCs are connected to the common dc-link, this instantaneous potential difference appears across the closed path and gives rise to the circulating current. In order to reduce the losses, the circulating should be suppressed to some acceptable limit. The reduction in the circulating current can be achieved by introducing sufficiently high inductance in the circulating current path. The CI is typically used for this
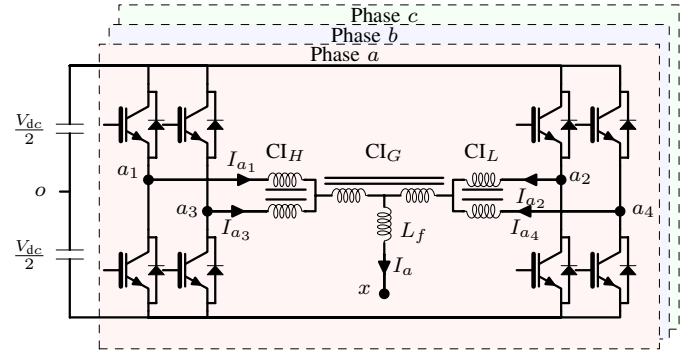
purpose [1], [11]–[16]. It provides magnetic coupling between the interleaved legs of a particular phase and offers high inductance to the circulating current, while its effect on the line current is minimal (considering negligible flux leakage).

The various possible arrangements of the CI for four parallel VSCs are shown in Fig. 2. Fig. 2(a) shows the magnetic structure of the CI with four parallel limbs. This magnetic structure is asymmetrical (for more than two limbs). The symmetry can be achieved by using a whiffletree configuration, as shown in Fig. 2(b). Two limb CI is used as a basic building block and the system arrangement, such as shown in Fig. 3, can be realized using it. Two interleaved VSC legs of a respective phase are magnetically coupled using the CI_H, whereas CI_L used to couple remaining two VSC legs (refer Fig. 3). The magnetic coupling between these two groups is achieved using the third CI (CI_G). One of the main advantages of the whiffletree configuration is the magnetically symmetrical structure of all CIs. However, it can only be only used for the even number of parallel VSCs. The integrated inductor is proposed for four parallel VSCs, which combines the functionality of the line filter inductor L_f and the CI_H and the CI_L (refer Fig. 2(b)) and it is presented in the following Section.

III. INTEGRATED INDUCTOR

The system comprises of four parallel VSCs with the proposed integrated inductor is shown in Fig. 4(a). All four VSCs share a common dc-link and the carrier signals are symmetrically interleaved, i.e. the carrier signals are phase shifted from each other by $90°$. The carrier signals of the VSC1 and VSC3 are phase shifted by $180°$ from each other and these two VSCs form the High-Side Converter Group (HSCG). Similarly, VSC2 and VSC4 forms the Low-Side Converter Group (LSCG), and use the carrier signals that are phase shifted from each other by $180°$.

The proposed integrated inductor for such systems is shown in Fig. 5, where two different core geometries are shown. The magnetic structure comprises of two cells. The cell is a two limb CI structure and each limb carries a coil with N number of turns. Both of these coils in the given cell are wound in the same direction. The limbs are magnetically coupled to each other using the top and the bottom yokes.
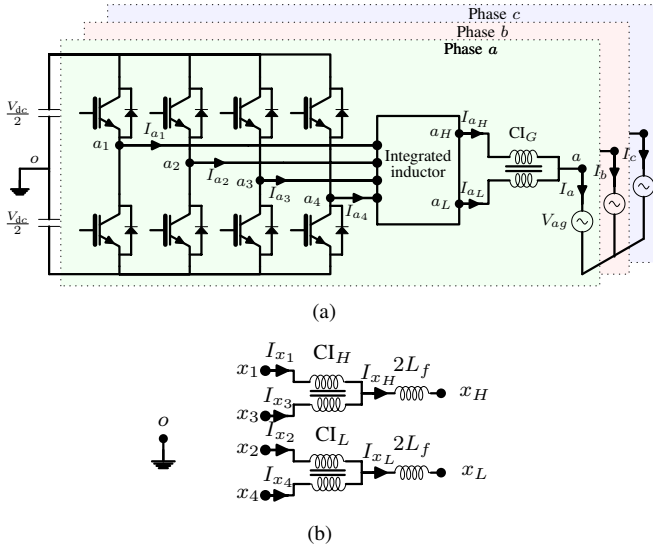
(a)

(b)

Fig. 4. Four parallel interleaved VSCs with the proposed integrated inductor. (a) System schematic, (b) Equivalent electrical model of the integrated inductor. The subscript x represents phases $x = \{a, b, c\}$.
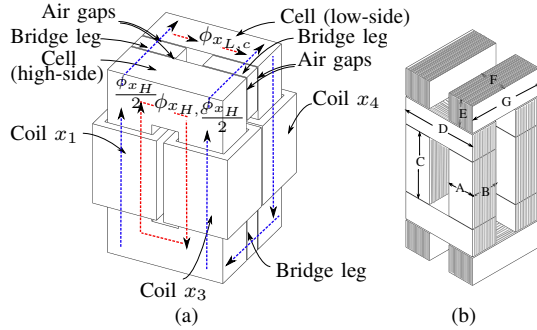

(a) (b)

Fig. 5. Magnetic structures of the proposed integrated inductor. Two different arrangements of the bridge legs are shown. Based on the direction of the laminations, one of the arrangement can be used. The subscript x represents the phase, $x = \{a, b, c\}$ (a) Suitable for the ferrite cores. It can be also used when the cells are made from the tape wound core, (b) Suitable for the laminated cores.

Out of these two cells, one of the cells magnetically couples the interleaved legs of the respective phases of the HSCG, whereas the other cell belongs to the LSCG. The input terminals of the coils of the high-side cell are connected to the output of VSC1 (x_1) and VSC3 (x_3) and the output terminals of these coils are connected together to form the common output x_H. Similarly, the output of VSC2 (x_2) and VSC4 (x_4) are connected to the input terminal of the coils of the low-side cell. Whereas, the other end of the coils are connected together to form the common output terminal x_L. The winding direction of the coils of the high-side cell is opposite to that of the coils of the low-side cell. The high-side and the low-side cells are magnetically coupled to each other using the bridge legs, as shown in Fig. 5(a). The necessary air gaps have been inserted between the cells and the bridge legs. The output terminals of the HSCG and the LSCG are connected to another CI (CI$_G$), as shown in Fig. 4(a).
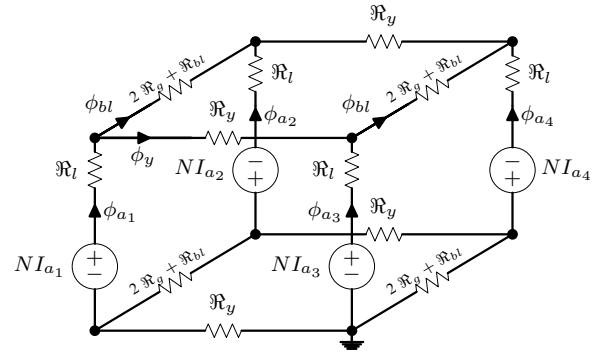

Fig. 6. Simplified reluctance model of the proposed integrated inductor.

A. Magnetic Circuit Analysis

The integrated inductor is analyzed in this sub section. Due to the phase symmetry, the analysis is presented for one of the phases, which is denoted by the subscript x. For the brevity, the permeability of the magnetic material is assumed to be constant and the leakage flux is neglected. For the system shown in Fig. 4(a), the voltage across the coil x_1 is given as

$$V_{x_1 x_H} = L_{x_1 x_1}\frac{dI_{x_1}}{dt} + L_{x_1 x_2}\frac{dI_{x_2}}{dt} + L_{x_1 x_3}\frac{dI_{x_3}}{dt} + L_{x_1 x_4}\frac{dI_{x_4}}{dt} \quad (1)$$

where $L_{x_j x_k}$ is the inductance between the jth and the kth coil of the integrated inductor of phase x and I_{x_n} is the current flowing through the nth coil of phase x. The simplified reluctance model of the integrated inductor is shown in Fig. 6. The reluctance of each of the limbs and the yoke of the cell are represented by $\Re_l$ and $\Re_y$, respectively. The reluctance of the bridge leg is $\Re_{bl}$, whereas the reluctance of each of the air gaps is denoted by $\Re_g$. The magneto-motive force of the coil is represented as NI_{x_n}, where N is the number of turns.

By solving the reluctance network, the flux in each limb can be obtained as

$$\overrightarrow{\phi} = \frac{1}{\Re_l}\boldsymbol{R}(\frac{1}{\Re_l}\boldsymbol{A} + \boldsymbol{R^{-1}})\overrightarrow{\boldsymbol{M}} \quad (2)$$

where $\boldsymbol{A}$ is the unit matrix,

$$\overrightarrow{\phi} = \begin{bmatrix} \phi_{x_1} & \phi_{x_2} & \phi_{x_3} & \phi_{x_4} \end{bmatrix}^T \quad (3)$$

$$\overrightarrow{\boldsymbol{M}} = \begin{bmatrix} NI_{x_1} & -NI_{x_2} & NI_{x_3} & -NI_{x_4} \end{bmatrix}^T \quad (4)$$

$$\boldsymbol{R} = \begin{bmatrix} \frac{1}{\Re_{eq}} & -\frac{1}{\Re_2} & -\frac{1}{\Re_1} & 0 \\ -\frac{1}{\Re_2} & \frac{1}{\Re_{eq}} & 0 & -\frac{1}{\Re_1} \\ -\frac{1}{\Re_1} & 0 & \frac{1}{\Re_{eq}} & -\frac{1}{\Re_2} \\ 0 & -\frac{1}{\Re_1} & -\frac{1}{\Re_2} & \frac{1}{\Re_{eq}} \end{bmatrix} \quad (5)$$

where $\Re_1 = 2\Re_y$, $\Re_2 = 4\Re_g + 2\Re_{bl}$, and $\frac{1}{\Re_{eq}} = \frac{1}{\Re_1} + \frac{1}{\Re_2}$. The reluctance of the air gap is very large compared to the reluctance of the bridge legs ($\Re_g >> \Re_{bl}$). Therefore $\Re_2 \approx 4\Re_g$. The limbs and the yokes of the cell are made from the same magnetic material and let $\Re_1$ to be equal to $\alpha\Re_l$. The flux linking with each of the coils is obtained by solving (2) and the inductances between the coils are obtained from the associated flux linkages. For most of the commercially available cell structures, the ratio of the window height to window width varies from 2 to 3. In this case, α can be safely

assumed to be equal to 1. With $\alpha = 1$, the inductance values are obtained as

$$L_{x_1 x_1} = L_S = \frac{N^2(2\Re_1^2 + 13\Re_1\Re_g + 12\Re_g^2)}{3\Re_1(\Re_1 + 2\Re_g)(\Re_1 + 6\Re_g)}$$

$$L_{x_1 x_2} = L_{M_1} = \frac{N^2(\Re_1 + 5\Re_g)}{3(\Re_1 + 2\Re_g)(\Re_1 + 6\Re_g)}$$

$$L_{x_1 x_3} = L_{M_2} = -\frac{N^2(\Re_1^2 + 8\Re_1\Re_g + 24\Re_g^2)}{6\Re_1(\Re_1 + 2\Re_g)(\Re_1 + 6\Re_g)}$$ (6)

$$L_{x_1 x_4} = L_{M_3} = \frac{N^2(\Re_1 + 8\Re_g)}{6(\Re_1 + 2\Re_g)(\Re_1 + 6\Re_g)}$$

Substituting these inductance values in (1) yields

$$V_{x_1 x_H} = V_{x_1 o} - V_{x_H o}$$
$$= L_S \frac{dI_{x_1}}{dt} + L_{M_1}\frac{dI_{x_2}}{dt} + L_{M_2}\frac{dI_{x_3}}{dt} + L_{M_3}\frac{dI_{x_4}}{dt}$$ (7)

Using the same procedure for the remaining coils, the voltage across each of the coils are obtained as

$$\overrightarrow{V_c} = L\frac{d\overrightarrow{I_c}}{dt}$$ (8)

where

$$\overrightarrow{V_c} = \begin{bmatrix} V_{x_1 x_H} & V_{x_2 x_L} & V_{x_3 x_H} & V_{x_4 x_L} \end{bmatrix}^T$$
$$= \begin{bmatrix} V_{x_1 o} - V_{x_H o} & V_{x_2 o} - V_{x_L o} & V_{x_3 o} - V_{x_H o} & V_{x_4 o} - V_{x_L o} \end{bmatrix}^T$$
(9)

$$\overrightarrow{I_c} = \begin{bmatrix} I_{x_1} & I_{x_2} & I_{x_3} & I_{x_4} \end{bmatrix}^T$$ (10)

and

$$L = \begin{bmatrix} L_S & L_{M_1} & L_{M_2} & L_{M_3} \\ L_{M_1} & L_S & L_{M_3} & L_{M_2} \\ L_{M_2} & L_{M_3} & L_S & L_{M_1} \\ L_{M_3} & L_{M_2} & L_{M_1} & L_S \end{bmatrix}$$ (11)

Each of the coil currents has two distinct components

1) Common current component that contributes to the output current
2) Circulating current component

The sum of the common current component of each of the VSCs withing the converter group constitutes the output current of the corresponding converter group. Therefore, the output currents of the HSCG and the LSCG are

$$I_{x_H} = I_{x_1} + I_{x_3}$$
$$I_{x_L} = I_{x_2} + I_{x_4}$$ (12)

Assuming equal current sharing between the VSCs, the common component of each of the VSCs is taken to be the same. Therefore, the output current of the individual VSCs are given as

$$I_{x_1} = \frac{I_{x_H}}{2} + I_{x_{H,c}}$$

$$I_{x_3} = \frac{I_{x_H}}{2} - I_{x_{H,c}}$$
(13)
$$I_{x_2} = \frac{I_{x_L}}{2} + I_{x_{L,c}}$$
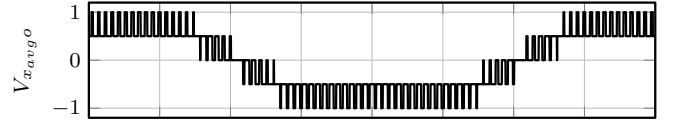
$$I_{x_4} = \frac{I_{x_L}}{2} - I_{x_{L,c}}$$

Fig. 7. Voltage waveform of an average voltage $V_{x_{avg}o}$, which exhibits five-level voltage waveforms. The VSCs are modulated using the space vector modulation with the modulation index $m = 0.8$. The average voltage is normalized to half of the dc-link voltage $\frac{V_{dc}}{2}$.

where $I_{x_{H,c}}$ and $I_{x_{L,c}}$ are the circulating current between the VSCs of the HSCG and the LSCG, respectively and given as

$$I_{x_{H,c}} = \frac{I_{x_1} - I_{x_3}}{2}$$ (14)

similarly

$$I_{x_{L,c}} = \frac{I_{x_2} - I_{x_4}}{2}$$ (15)

The sum of the output currents of the HSCG and the LSCG constitutes the resultant line current and it is given as

$$I_x = I_{x_L} + I_{x_H}$$ (16)

and the circulating current between the high-side and the low-side converter groups is given as

$$I_{x,c} = \frac{I_{x_H} - I_{x_L}}{2}$$ (17)

The circulating current between the HSCG and the LSCG ($I_{x,c}$) is suppressed using the CI$_G$.

B. Inductance Offered by the Integrated Inductor

Using the induced voltages given in (8) and averaging the switched output voltages of the VSCs of the HSCG gives

$$\left(\frac{V_{x_1 o} + V_{x_3 o}}{2}\right) - V_{x_H o} = \left(\frac{L_S + L_{M_2}}{2}\right)\frac{d(I_{x_1} + I_{x_3})}{dt} + \left(\frac{L_{M_1} + L_{M_3}}{2}\right)\frac{d(I_{x_2} + I_{x_4})}{dt}$$ (18)

similarly, averaging the switched output voltages of the VSCs of the LSCG yields

$$\left(\frac{V_{x_2 o} + V_{x_4 o}}{2}\right) - V_{x_L o} = \left(\frac{L_{M_1} + L_{M_3}}{2}\right)\frac{d(I_{x_1} + I_{x_3})}{dt} + \left(\frac{L_S + L_{M_2}}{2}\right)\frac{d(I_{x_2} + I_{x_4})}{dt}$$ (19)

Using (12) and averaging (18) and (19) yields

$$V_{x_{avg}o} - V_{xo} = \left(\frac{L_S + L_{M_1} + L_{M_2} + L_{M_3}}{4}\right)\frac{d(I_{x_H} + I_{x_L})}{dt}$$ (20)

where

$$V_{x_{avg}o} = \frac{1}{4}\sum_{k=1}^{4} V_{x_k o}$$ (21)

and

$$V_{xo} = \frac{V_{x_H o} + V_{x_L o}}{2}$$ (22)

The waveform of the average voltage $V_{x_{avg}o}$ is shown in Fig. 7. The $V_{x_{avg}o}$ exhibits five-level voltage waveforms and the voltage difference of $V_{x_{avg}o} - V_{xo}$ appears across the integrated inductor. The integrated inductor offers desired value of the

inductance L_f to the line current I_x and it the the voltage $V_{x_{avg}o} - V_{xo}$ along with the L_f determines the ripple content in the I_x. The dynamic behavior of the I_x can be represented as

$$V_{x_{avg}o} - V_{xo} = L_f \frac{dI_x}{dt} \qquad (23)$$

Using (16) and (20), the line filter inductance can be obtained as

$$L_f = \frac{L_S + L_{M_1} + L_{M_2} + L_{M_3}}{4}$$
$$= \frac{N^2}{4(\Re_1 + 2\Re_g)} = \frac{N^2}{8\Re_g(1 + \frac{\Re_1}{2\Re_g})} \qquad (24)$$

As $\Re_g >> \Re_1$, the line filter inductance can be approximated as

$$L_f = \frac{\mu_0 N^2 A_g'}{8l_g} \qquad (25)$$

where μ_0 is the permeability of the free space, l_g is the length of the air gap, and A_g' is the effective cross-section area of the air gap. The effective cross-sectional area of the air gap $A_{g'}$ is obtained by evaluating the cross-section area of the air gap after adding l_g to each dimension in the cross-section.

The switched output voltage difference of VSC1 and VSC3 ($V_{x_1o} - V_{x_3o}$) drives the $I_{a_H,c}$. Similarly, the behavior of the $I_{a_L,c}$ depends on the difference of the switched output voltages of VSC2 and VSC4 ($V_{x_2o} - V_{x_4o}$). Using (8), the difference of the switched output voltages of the VSC1 and VSC3 ($V_{x_1o} - V_{x_3o}$) is obtained as

$$V_{x_1o} - V_{x_30} = (L_s - L_{M_2})\frac{d(I_{x_1} - I_{x_3})}{dt} + (L_{M_1} - L_{M_3})\frac{d(I_{x_2} - I_{x_4})}{dt} \qquad (26)$$

Using (6), (26), (14), and (15), the inductance offered to the circulating currents is given as

$$\begin{bmatrix} V_{x_1o} - V_{x_30} \\ V_{x_2o} - V_{x_40} \end{bmatrix} = \boldsymbol{L_c} \frac{d}{dt}\begin{bmatrix} I_{x_H,c} \\ I_{x_L,c} \end{bmatrix} \qquad (27)$$

where the circulating current inductance matrix $\boldsymbol{L_c}$ is given as

$$\boldsymbol{L_c} = 2\begin{bmatrix} L_s - L_{M_2} & L_{M_1} - L_{M_3} \\ L_{M_1} - L_{M_3} & L_s - L_{M_2} \end{bmatrix} \qquad (28)$$

where $L_s - L_{M_2} = \frac{2N^2}{3\Re_1}$ and $L_{M_1} - L_{M_3} = \frac{N^2}{36\Re_g}$. As $\Re_g >> \Re_1$, the circulating current inductance matrix can be approximated as

$$\boldsymbol{L_c} \approx 2\begin{bmatrix} \frac{2N^2}{3\Re_1} & 0 \\ 0 & \frac{2N^2}{3\Re_1} \end{bmatrix} \qquad (29)$$

C. Flux Density Analysis

The integrated inductor combines the functionalities of two CIs (CI_H and CI_L) and the line filter inductor L_f. Therefore, the flux in the magnetic core has distinct components corresponding to these inductances and it is analyzed in this sub section.
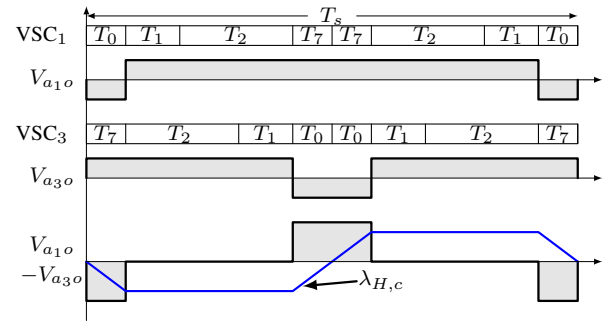

Fig. 8. Pole voltages of phase a of VSC1 and VSC3 and their difference for space vector modulation. The modulation index $M = 1$ and voltage space vector angle $\psi = 45°$. Time T_o, T_1, T_2, and T_7 are the dwell times of the corresponding voltage vectors.
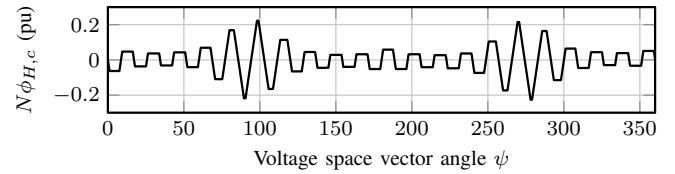

Fig. 9. Circulating flux component $\lambda_{H,c}$ over a complete fundamental period. The flux linkage is normalized to $V_{dc}T_s$.

1) Circulating Flux Component: The circulating flux linkage in the HSCG cell can be obtained as [17], [18]

$$\lambda_{x_H,c} = N\phi_{x_H,c} = \frac{1}{2}\int (V_{x_1o} - V_{x_3o})\,dt \qquad (30)$$

where $\phi_{x_H,c}$ is the circulating flux component in the high-side cell of the integrated inductor. The carrier signals of the VSC1 and VSC3 are interleaved by $180°$ and the corresponding voltages for a particular switching cycle is shown in Fig. 8. The VSCs are modulated using the space vector modulation [19]. Due to the change in the dwell time of the voltage vectors in each sampling interval, the peak value of the $\lambda_{x_H,c}$ also attains different values in each of the sampling intervals, as shown in Fig. 9. The $\lambda_{x_H,c}$ achieves the maximum value for the voltage space vector angle $\psi = 90°$ (and $\psi = 270°$), as shown in Fig. 9 and it is obtained as

$$\lambda_{x_H,c_{max}} = N\phi_{x_H,c_{max}} = \frac{V_{dc}}{8f_s} \qquad (31)$$

where V_{dc} is the dc-link voltage, f_s is the switching frequency, and $\phi_{H,c_{max}}$ is the maximum value of the circulating flux component.

For the LSCG, the carrier signals of the VSC2 and the VSC4 are also interleaved by $180°$ and the same analysis can be applied. The maximum value of the circulating flux component is also $N\phi_{x_L,c_{max}} = V_{dc}/8f_s$.

From the reluctance model, it is evident that the flux in the yokes of the cell is equal to the resultant component of the circulating flux component $\phi_y = \phi_{x_H,c} = \phi_{x_L,c}$. Therefore, the maximum value of the flux density in the yokes is

$$B_{y_{max}} = \frac{V_{dc}}{8NA_{c_y}f_s} \qquad (32)$$

where A_{c_y} is the cross section area of the yoke.

This article has been accepted for publication in a future issue of this journal, but has not been fully edited. Content may change prior to final publication. Citation information: DOI 10.1109/TPEL.2015.2514182, IEEE Transactions on Power Electronics

6

2) Common Flux Component: The common current component of each of the VSCs can be decomposed into:

1) Fundamental frequency component.
2) Major harmonic components at the $4kf_s$, where $k = 1, 2, .. \infty$.

As the common flux component is replica of the common current component, the common flux component is also comprised of a fundamental frequency component and a ripple component. The fundamental component of the common flux component is given as

$$\phi_r(t) = \frac{\mu_0 N A'_g}{8 l_g} I_{x_{max}} \cos(\psi + \theta) \quad (33)$$

Normally the line filter inductance value is selected to limit the peak-to-peak value of the ripple component of the line current to the desired value. Let the ratio of the peak-to-peak value of the ripple component of the line current to the amplitude of the fundamental component of the line current be ε. For the space vector modulation, the ripple component attains its maximum value at the space vector angle of $\psi = 0°$. For unity power factor applications, the fundamental component is also maximum at the $\psi = 0°$. Therefore, the common flux component also attains its maximum value at the space vector angle of $\psi = 0°$ and it is given as

$$\phi_{r_{max}} = (1 + \frac{\varepsilon}{2}) \frac{\mu_0 N A'_g}{8 l_g} I_{x_{max}} \quad (34)$$

where $I_{x_{max}}$ is the amplitude of the rated current. The common component of the flux ϕ_r completes its path through the bridge legs, air gaps and legs of the cells. Therefore, the maximum value of the flux density in the bridge leg is given as

$$B_{bl_{max}} = (1 + \frac{\varepsilon}{2}) \frac{\mu_0 N A'_g}{8 l_g A_{c_{bl}}} I_{x_{max}} \quad (35)$$

where $A_{c_{bl}}$ is the cross section area of the bridge leg.

3) Flux in the limbs of the cells: The flux in the limbs is the addition of the circulating flux component and the resultant flux component and it is given as

$$\phi_l(t) = \phi_r(t) + \phi_{x_{H,c}}(t) \quad (36)$$

for the unity power factor applications ($\theta = 0$), the common component of the flux is maximum for $\psi = 0°$, whereas the circulating flux component $\phi_{x_{H,c}}$ is minimum at this voltage space vector angle. Similarly, the $\phi_{x_{H,c}}$ is maximum at $\psi = 90°$ and the common flux component is zero. Therefore, for the unity power factor applications

$$\phi_{l_{max}} = \max(\phi_{x_{H,c_{max}}}, \phi_{r_{max}} + \phi_{x_{H,c}|_{\psi=0°}}) \quad (37)$$

IV. CIRCULATING CURRENT SUPPRESSION BETWEEN THE TWO CONVERTER GROUPS

The resultant output voltages of both the HSCG and LSCG are also phase-shifted with respect to each other and the circulating current flows between them due to these phase-shifted voltages. Additional CI (CI_G) is used to suppress this current.

The flux linkage in the CI_G is given as

(a)

(b)

(c)
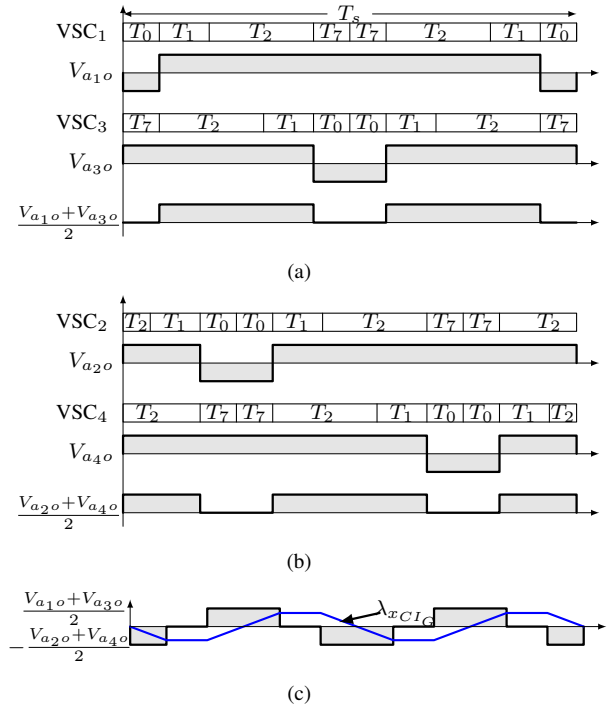
Fig. 10. Voltage waveforms for four parallel interleaved VSCs for the modulation index $M = 1$ and space vector angle $\psi = 45°$. (a) Pole voltages of the individual VSCs and their average voltage of the high side converter group, (b) Pole voltages of the individual VSCs and their average voltage of the low side converter group, (c) The difference of the average voltages of the high side converter group and the low side converter group and their associated flux linkage.
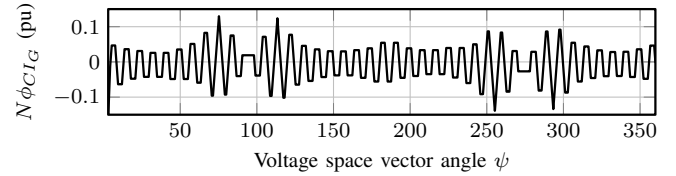

Fig. 11. Flux linkage of the CI_G ($\lambda_{x_{CI_G}}$) over a complete fundamental period. The flux linkage is normalized to $V_{dc} T_s$.

$$N\phi_{x_{CI_G}} = \frac{1}{2} \int \left((\frac{V_{x_{1o}} + V_{x_{3o}}}{2}) - (\frac{V_{x_{2o}} + V_{x_{4o}}}{2}) \right) dt \quad (38)$$

The pole voltages of the individual VSCs and their average voltage for both the HSCG and the LSCG are shown in Fig. 10(a) and 10(b), respectively. The difference in the average voltages of both the converter groups and flux linkage of the CI_G is shown in Fig. 10(c). The flux linkage behavior over a fundamental period is also shown in Fig. 11. The flux reversal in the CI_G is $2 \times f_s$ and subjected to the half of the dc-link voltage, which is also evident in Fig. 10(c). The maximum value of the flux linkage in the CI_G is given as

$$N_{CI_G} \phi_{CI_G,max} = \frac{V_{dc}}{32 f_s} \quad (39)$$

where N_{CI_G} is the number of turns in each of the coils of the CI_G and $\phi_{CI_G,max}$ is the maximum value of the flux in the CI_G. Using (30) and (39), the ratio of the flux linkage in the

TABLE I
SYSTEM PARAMETERS FOR SIMULATION AND EXPERIMENTAL STUDIES

Parameters	Values
Total power S	11 kVA
No. of VSCs	4
Interleaving angle	90°
DC-link voltage V_{dc}	650 V
Switching frequency f_s	1250 Hz
PWM scheme	Space vector modulation
Line filter inductance L_f	2.3 mH (0.05 pu)

TABLE II
DIMENSIONS OF THE IMPLEMENTED INDUCTOR (REFER FIG. 5(B))

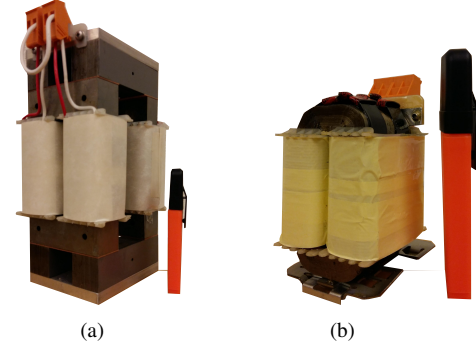| Parameters	A,B,E,F	C	D,G	l_g
Values (mm/mm^2)	25	75	85	1.0

(a)   (b)

Fig. 12. Pictures of the implemented inductor. (a) Integrated inductor, (b) Coupled inductor to suppress the circulating current between the high-side converter group and the low-side converter group (CI$_G$).

CI_G to the flux linkage in the CI_H (or CI_L) is given as

$$\frac{N_{CI_G}\phi_{CI_{G,max}}}{N\phi_{x_{H,c}}} = \frac{1}{4} \tag{40}$$

as it is evident form (40), the size of the CI_G is approximately 25% than that of the CI_H. The maximum value of the flux density in the CI_G is given as

$$B_{CI_{G,max}} = \frac{V_{\text{dc}}}{32 N_{CI_G} A_{c_{CI_G}} f_s} \tag{41}$$

where $A_{c_{CI_G}}$ is the cross section area of the CI_G.

V. FINITE ELEMENT ANALYSIS AND COMPARATIVE EVALUATION

The size reduction achieved by the magnetic integration is demonstrated by comparing the volume of the proposed solution with the volume of the magnetic components of the system proposed in [1], [20] and also shown in Fig. 2(b).

A. Finite Element Analysis

The simplified reluctance model is used for the analysis, which does not take into account the effects of the flux leakage. Therefore, (25) gives underestimated value as the total inductance offered to the line current is given by

$$L_{\text{line}} = L_f + \frac{L_{\sigma,II}}{4} + \frac{L_{\sigma,CI_G}}{2} \tag{42}$$

where $L_{\sigma,II}$ and L_{σ,CI_G} are the leakage inductances of the integrated inductor and the CI_G, respectively. On the other hands, inherent air gap exists in the cell structure due to the core joints, which tends to decrease the value of the L_f. Therefore the design equations derived in section IV can be used to get the parameters for the first design iteration and Finite Element Analysis (FEA) should be carried out in order to fine tune those design parameters.

The integrated inductor and the CI_G is designed using the design equations derived in section III and section IV for the converter system with four parallel VSCs. The system parameters are given in Table I. Amorphous alloy 2605SA1 is used for the cells of integrated inductor and for the CI_G core, whereas laminated steel with a lamination thickness of 0.35 mm is used for the bridge legs. The cells of the integrated inductor are constructed using four blocks. Due to the use of the laminated cores, the magnetic structure shown in Fig. 5(b) is used (to avoid large eddy current losses in the core).

The dimensions of the implemented inductors are specified in Table II. The integrated inductor is assembled using the
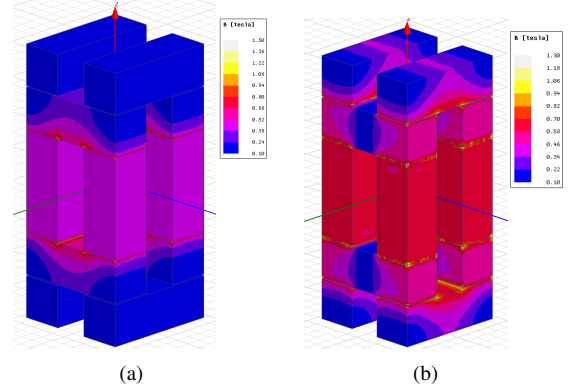

(a)   (b)

Fig. 13. The flux density distribution in the magnetic core. (a) Phase shifted components of switched output voltage of the carrier frequency harmonics are applied across the coils, (b) Coils are excited with the common component of the current.

core blocks available in the laboratory. The stacking factor for the amorphous core blocks is taken to be 0.89, whereas it is assumed to be 0.96 for the laminated steel. The coils are wound using the AWG 16 enameled copper wire with the cross section area $A_{cu} = 1.31 \times 10^{-6}$ m^2. Each of the coils has 140 number of turns. The picture of the implemented integrated inductor is shown in Fig. 12(a).

The finite element analysis has been carried out using Ansys Maxwell and the flux density distribution in the magnetic core is shown in Fig. 13. The flux is mainly confined to the corresponding cells when the coils are excited with the phase shifted components of switched output voltage of the carrier frequency harmonics, as shown in Fig. 13(a). On the other hand, the induced flux of coils of the HSCG cell links with the coils of the LSCG cell and vice-versa when the coils are excited with the common component of the current. As a result, the common component of the flux completes its path through the bridge legs and the air gaps, as shown in Fig. 13(b).

The inductance values are obtained using the FEA and

TABLE III
INDUCTANCE VALUES OBTAINED USING THE FINITE ELEMENT ANALYSIS

Inductance	L_s	L_{m_1}	L_{m_2}	L_{m_3}
Values (mH)	29.6	2.6	-22.3	2.5

TABLE IV
DESIGN PARAMETERS OF THE COUPLED INDUCTOR CI_G

Parameters	Values
Cross-section area of the core $A_{c_{CI}}$	4.6×10^{-4} m^2
Number of turns N_{CI}	53
Cross section area of the conductor A_{cu}	2.62×10^{-6} m^2 (AWG 13)

they are given as given Table III. The inductance offered to the line current is then calculated to be 3.1 mH using (24). The circulating current inductance matrix $\boldsymbol{L_c}$ is calculated as

$$\boldsymbol{L_c} = 2 \begin{bmatrix} 52 & 5.1 \\ 5.1 & 52 \end{bmatrix} \text{mH} \tag{43}$$

The circulating current between the HSCG and the LSCG is suppressed using the CI_G. The CI_G is realized using the POWERLITE C-cores form the Metglas. Two AMCC16-B cores are stacked together to achieve core cross-section area of 4.6×10^{-4} m^2. The FEA has been carried out for the CI_G and the inductance matrix calculated and it is given as

$$\boldsymbol{L}_{\text{CI}_G} = \begin{bmatrix} 3.5 & -3.27 \\ -3.27 & 3.5 \end{bmatrix} \text{mH} \tag{44}$$

Therefore the inductance offered to the line current by the leakage inductance of the CI_G is 0.1 mH and the inductance offered to the circulating current between the HSCG and the LSCG is 13.54 mH.

B. Comparative Evaluation

The volume of the different active materials of the proposed filter arrangement is compared with the volume of the state-of-the-art solution, shown in Fig. 2(b) for the the system parameters specified in the Table I. Moreover, the losses in the magnetic components in both the cases are also compared.

The bridge legs of the integrated inductor and the line filter inductor in Fig. 2(b) is assumed to be made from the 0.35 mm laminated silicon steel, whereas the amorphous alloys 2605SA1 is considered as a magnetic material for the cells of the integrated inductor and for the CI_H, CI_L, and CI_G in Fig. 2(b). As the core losses in the amorphous alloys 2605SA1 is lower compared to the laminated silicon steel, it is used for cells of the magnetic structures which carry the switching frequency circulating flux component. However, the price of the amorphous alloys 2605SA1 is higher compared to the laminated silicon steel. Therefore to reduce the cost, laminated silicon steel is used for the bridge legs, which carry the common flux component with predominant fundamental frequency component. The design of the CI_G that is used to suppress the current between the HSCG and the LSCG is taken to be the same in both cases. The flux densities in the cores and the current density in the coils are taken to be the same in both the cases.

TABLE V
VOLUME COMPARISON OF THE ACTIVE MATERIALS OF THE MAGNETIC COMPONENTS IN THE PROPOSED SOLUTION WITH THE STATE-OF-THE-ART SOLUTION SHOWN IN FIG. 2(B)

Material	State-of-the-art	Proposed	% reduction
Amorphous alloy 2605SA1	1.477 Ltr.	1.221 Ltr.	17.3%
Laminated steel	1.28 Ltr.	0.63 Ltr.	49%
Copper	0.385 Ltr.	0.337 Ltr.	12.4 %

TABLE VI
STEINMETZ PARAMETERS OF THE AMORPHOUS ALLOYS 2605SA1 AND THE LAMINATED SILICON STEEL

Material	k_i	α	β
Amorphous alloy 2605SA1	0.62	1.51	1.74
Laminated steel	0.96	1.55	1.87

1) Volumetric Comparison: The volume of the different materials in both the cases for all the three phases are given in Table V. In the filter arrangement shown in Fig. 2(b), the windings of the line filter inductor carries full line current and it is completely eliminated in the proposed solution. Therefore, the designer may choose to increase the number of turns in the coils of the integrated inductor to reduce the size of the amorphous alloy. In this comparison, the number of turns in the integrated inductor is taken to be 10% higher than the number of turns in the CI_H and CI_L in the filter arrangement shown in Fig. 2(b). This results in the 17.3% saving in the amorphous alloy and 12.4% reduction in copper. Furthermore, the volume of the laminated steel is reduced by 49% in the proposed solution.

2) Losses Comparison: The Improved Generalized Steinmetz Equation (IGSE) [21], [22] is used to calculate the core losses. The core losses per unit volume is given as

$$P_{fe,v} = \frac{1}{T} \int_0^T k_i \left| \frac{dB(t)}{dt} \right|^\alpha (\Delta B)^{\beta - \alpha} dt \tag{45}$$

where ΔB is the Peak-to-peak value of the flux density. α, β and k_i are the constants determined by the material characteristics. These constants for both the amorphous alloys and the laminated silicon steel are given in Table VI. The flux waveform has major and minor loops and the core losses due to these loops are evaluated separately.

The copper loss is evaluated by considering the ac resistance of the winding, which takes into account the skin and proximity effects [23]. The total winding losses are given as

$$P_{cu} = R_{dc} \sum_{h=1}^\infty k_{p_h} I_h^2 \tag{46}$$

where

$$k_{p_h} = \sqrt{h}\Delta \left[\frac{\sinh(2\sqrt{h}\Delta) + \sin(2\sqrt{h}\Delta)}{\cosh(2\sqrt{h}\Delta) - \cos(2\sqrt{h}\Delta)} \right. $$
$$\left. + \frac{2}{3}(m^2 - 1)\frac{\sinh(\sqrt{h}\Delta) - \sin(\sqrt{h}\Delta)}{\cosh(\sqrt{h}\Delta) + \cos(\sqrt{h}\Delta)} \right] \tag{47}$$

and $\Delta = T_c/\delta$. R_{dc} is the dc resistance of the coil, m is the number of layers in the coil, I_h is the hth harmonic component

TABLE VII
CORE AND COPPER LOSSES COMPARISON. THE LOSSES OF ALL THE
THREE PHASES ARE LISTED.

Item	load	State-of-the-art	Proposed	% reduction
Core losses (W)	0.5 pu	35.6	27.3	23%
	1 pu	39.8	29	27%
Copper losses (W)	0.5 pu	21.5	15.1	29%
	1 pu	76.3	55.8	26%

of the leg current. T_c is the thickness of the coil and δ is the skin depth.

The core and the copper losses of the proposed integrated inductor are evaluated and the total losses of all the three integrated inductor (for three phase system) are given in Table VII. The inductor losses in the case of the state-of-the-art solution are also evaluated at the 50% of the rated load and 100% of the rated load conditions. The losses in the integrated inductor are low compared to the state-of-the-art solution at both the loading conditions. The total losses in the integrated inductors at the rated load conditions are 84.8 W, compared to the 116.1 W in the case of the state-of-the-art solutions (27% reduction). The worst case losses in one integrated inductor is 28.2 W (84.8/3 W), out of which 18.6 W is the total copper losses in all the four coils. Since the coils are exposed to the ambient air, the generated heat can be easily dissipated through natural convection.

VI. SIMULATION AND THE EXPERIMENTAL RESULTS

The simulation and the experimental results for the four parallel interleaved VSCs are presented in this section for the system parameters specified in Table I.

A. Simulation Results

The time domain simulation has been carried out using PLECS, where the simplified model of the integrated inductor, shown in Fig. 6, has been implemented using the permeance-capacitance analogy. The simulated flux density waveforms in the various parts of the magnetic structure of the integrated inductor and the CI_G are shown in Fig. 14 and Fig. 15, respectively. Fig. 14(a), shows the flux density waveform in the limb of the cell, which is a vector addition of the common flux component and the circulating flux component. The circulating flux is confined to the cell and therefore the flux in the yoke has a switching frequency component as a major harmonic component, which is shown in Fig. 14(b). The common flux component flows out of the cell and completes its path through the air gaps and the bridge leg, as shown in Fig. 14(c). Due to the magnetic integration, the common flux component of the cell of the HSCG completes its path through the limbs of the cell of the LSCG and vice-versa. As a result, a dedicated return path is avoided. Moreover, for the unity power factor applications, the common flux component is maximum when the circulating flux component is minimum and vice-versa as shown in Fig. 14. As the flux in the limb is the addition of these two components, the cross section area of the limb can be made smaller compared to the individual inductor case. This leads to substantial reduction of the volume of the integrated
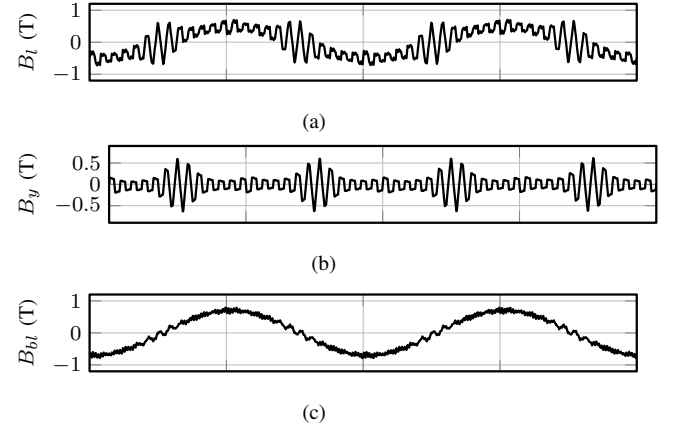

Fig. 14. Simulation results at rated operating conditions. (a) Flux density in the limb of the cell of the integrated inductor, (b) Flux density in yoke of the cell, (c) Flux density in the bridge leg.
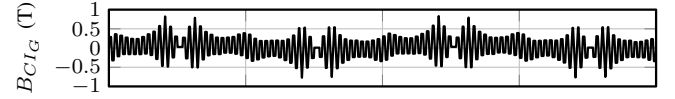

Fig. 15. Simulation results. (a) Flux density waveform in the coupled inductor that is used to suppress the circulating current between the high side and the low side converter group.
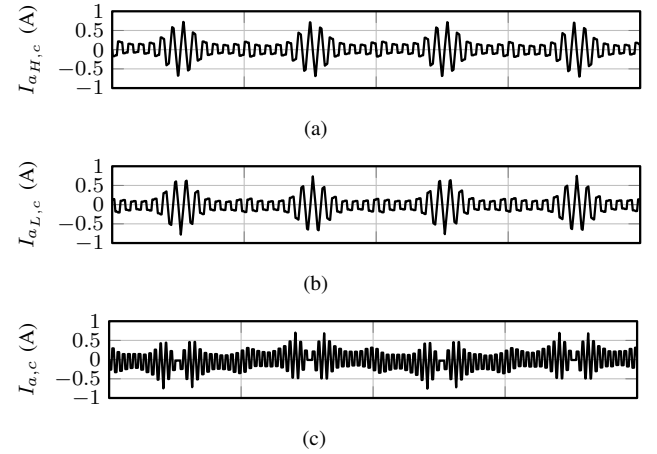

Fig. 16. Simulated current waveforms at rated operating conditions. (a) Circulating current between the VSCs of the high side converter group $I_{a_{H,c}}$, (b) Circulating current between the VSCs of the low side converter group $I_{a_{L,c}}$, (c) Circulating current between the high side converter group and the low side converter group $I_{a,c}$.

inductor.

The circulating current between the HSCG and the LSCG is suppressed using the CI_G. The CI_G is subjected to half of the dc-link voltage and the flux has a major harmonic component at the 2nd carrier harmonic component. The flux density in the CI_G is shown in Fig. 15, which demonstrates that the flux reversal takes place at twice the switching frequency.

The simulated circulating currents between the VSCs of the HSCG and between the VSCs of the LSCG are shown in Fig. 16(a) and Fig. 16(b), respectively. The integrated inductor offers high inductance to the circulating currents and suppresses them effectively. The additional CI_G is also very
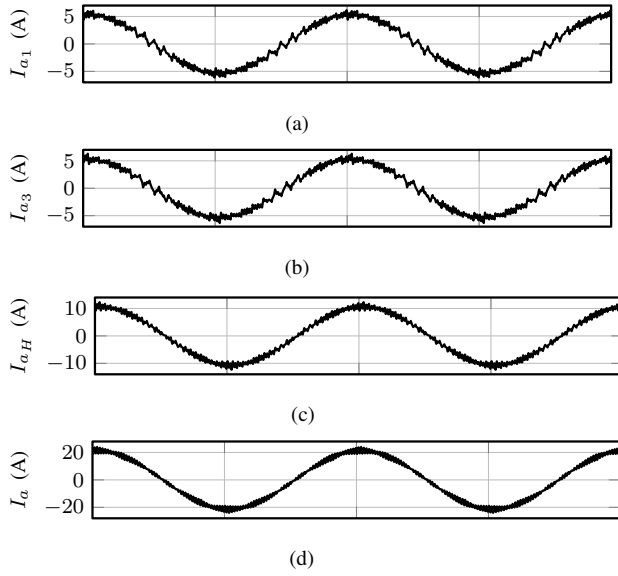
Fig. 17. Simulated current waveforms of phase a at rated operating conditions. (a) Output current VSC$_1$ (I_{a_1}), (b) Output current VSC$_3$ (I_{a_3}), (c) Resultant current of the high side converter group (I_{a_H}), (d) Line current I_a.
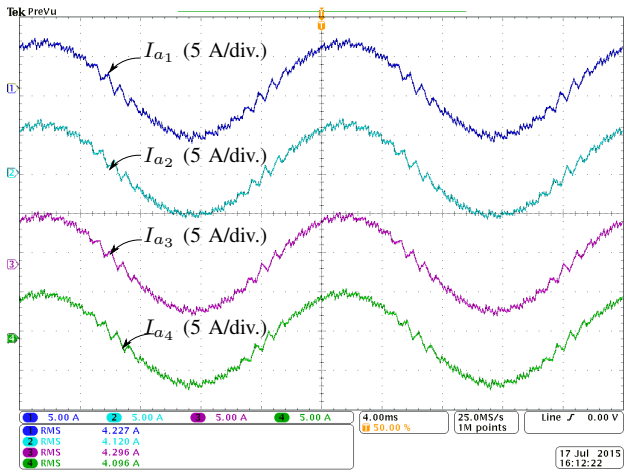

Fig. 18. Experimental waveforms of the phase a of the output current of the individual VSCs. (a) Ch1: Output current of VSC$_1$ (I_{a_1}), Ch2: Output current of VSC$_2$ (I_{a_2}), Ch3: Output current of VSC$_3$ (I_{a_3}), Ch4: Output current of VSC$_4$ (I_{a_4}).

effective in suppressing the circulating current between the HSCG and the LSCG, as shown in Fig. 16(c).

The simulated currents of phase a are shown in Fig. 17. The output current of the VSCs of the HSCG are only shown. However, the output current of the VSCs of the LSCG also demonstrates similar current waveform quality. The line current is shown in Fig. 17(d), which has a very small ripple component. This demonstrates effective line current filtering functionality of the integrated inductor.

B. Experimental Results

The experimental results were obtained for the system specified in Table I. Four VSCs were connected in parallel. The carrier signals of these parallel connected VSCs were interleaved by an interleaving angle of $90°$. The VSCs
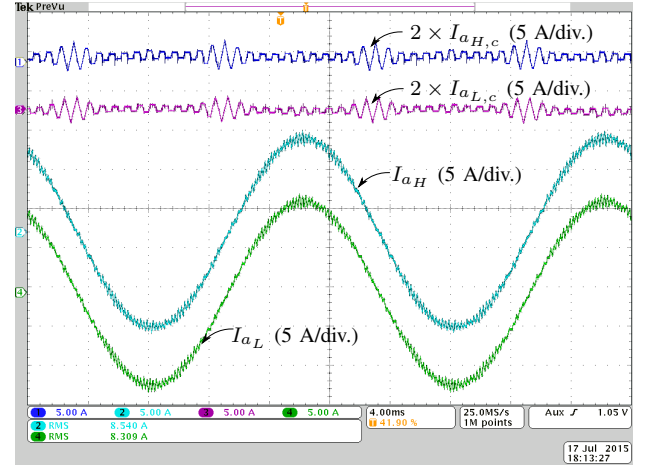

Fig. 19. Experimental waveforms of the phase a. (a) Ch1: Circulating current between the VSCs of the high-side converter group ($2 \times I_{a_{H,c}}$), Ch2: Output current of the high-side converter group (I_{a_H}), Ch3: Circulating current between the VSCs of the low-side converter group ($2 \times I_{a_{L,c}}$), Ch4: Output current of the low-side converter group (I_{a_L}).
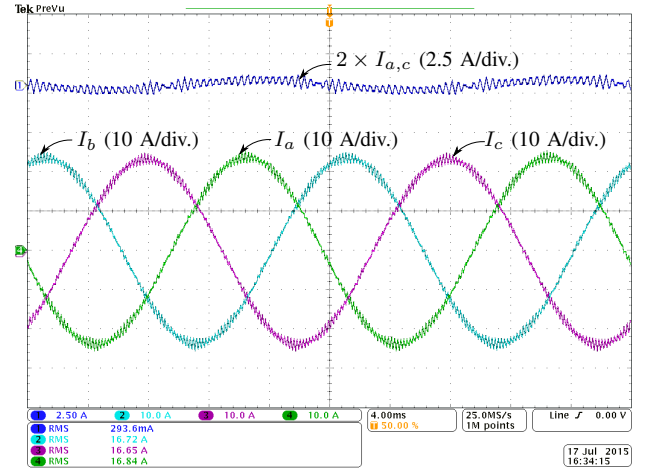

Fig. 20. Experimental waveforms. (a) Ch1: Circulating current between the high-side converter group and the low-side converter group ($2 \times I_{a,c}$), Ch2: Resultant line current of phase a (I_a), Ch3: Resultant line current of phase b (I_b), Ch4: Resultant line current of phase c (I_c).

were modulated using the space vector modulation, using TMS320F28346 floating-point digital signal processor. The dc-link was connected to the dc power supply and the ac-side is connected to the three-phase resistive load of 13.33 Ω.

The output current of phase a of the individual VSCs of both the HSCG and the LSCG is shown in Fig. 18. The individual VSCs are operated with the switching frequency of 1.25 kHz, and the switched output voltages of the individual VSCs has a major harmonic component at the carrier frequency harmonics. Due to the interleaved carrier signals, these voltage components are phase shifted and appears across the closed path formed due to the interleaved operation and the common dc-link. The integrated inductor offers the circulating current inductance to these voltage components. As it is evident from Fig. 19, the circulating current between the VSCs of the HSCG (as well as between the VSCs of the LSCG) is suppressed very effectively. This shows that the integrated inductor offers

high inductance to the phase shifted voltage components and effectively suppresses the circulating current.

The output current of both the HSCG and the LSCG along with their circulating currents are shown in Fig. 19. The measured peak value of the circulating current between the VSCs of the HSCG is 0.8 A, which is around 13% of the amplitude of the output current of the individual VSCs. The circulating current between the HSCG and the LSCG is effectively suppressed by the CI_G, as it is evident from Fig. 20. The resultant line current of all the three phases are also shown in Fig. 20. The integrated inductor also offers the desired inductance to the resultant line current, which demonstrates the line current filtering functionality of the integrated inductor.

VII. CONCLUSION

An integrated inductor for the parallel interleaved VSCs connected in a whiffletree configuration is proposed in this paper. The proposed integrated inductor suppresses the circulating current between the parallel interleaved VSCs. In addition, it offers the desired inductance to the line current as well. The converters are divided into a high-side converter group and a low-side converter group. The fundamental component of the flux in the cell of the high side converter group is equal to the fundamental component of the flux in the cell of the low-side converter group. Because of the unique arrangement of the coils in the proposed inductor, the fundamental component of the flux of the high-side converter group completes its path through the limbs of the cells of the low-side converter group. Therefore, the dedicated magnetic structure for the return path for the fundamental flux component is avoided. Moreover, the magnetic integration also leads to substantial size reduction of the limbs. As a result, compared to the state-of-the-art solution, 49% reduction in the volume of the laminated silicon steel, 17.3% reduction in the volume of the amorphous alloy, and 12.4% reduction in the volume of the copper can be achieved for the system parameters considered in this paper. The operation of the proposed system has been discussed and the losses are analyzed. The analysis is supported by the simulations and the experimental results.

ACKNOWLEDGMENT

REFERENCES

[1] F. Ueda, K. Matsui, M. Asao, and K. Tsuboi, "Parallel-connections of pulsewidth modulated inverters using current sharing reactors," *IEEE Trans. Power Electron.*, vol. 10, no. 6, pp. 673–679, Nov 1995.

[2] S. Miller, T. Beechner, and J. Sun, "A comprehensive study of harmonic cancellation effects in interleaved three-phase VSCs," in *Proc. IEEE Power Electronics Specialists Conference, 2007. PESC 2007.*, 2007, pp. 29–35.

[3] L. Asiminoaei, E. Aeloiza, P. N. Enjeti, and F. Blaabjerg, "Shunt active-power-filter topology based on parallel interleaved inverters," *IEEE Trans. Ind. Electron.*, vol. 55, no. 3, pp. 1175–1189, 2008.

[4] D. Zhang, F. Wang, R. Burgos, L. Rixin, and D. Boroyevich, "Impact of Interleaving on AC Passive Components of Paralleled Three-Phase Voltage-Source Converters," *IEEE Trans. Ind. Appl.*, vol. 46, no. 3, pp. 1042–1054, 2010.

[5] J. Prasad and G. Narayanan, "Minimization of Grid Current Distortion in Parallel-Connected Converters Through Carrier Interleaving," *IEEE Trans. Ind. Electron.*, vol. 61, no. 1, pp. 76–91, Jan 2014.

[6] X. Mao, A. Jain, and R. Ayyanar, "Hybrid interleaved space vector PWM for ripple reduction in modular converters," *IEEE Trans. Power Electron.*, vol. 26, no. 7, pp. 1954–1967, 2011.

[7] K. Xing, F. Lee, D. Borojevic, Z. Ye, and S. Mazumder, "Interleaved PWM with discontinuous space-vector modulation," *IEEE Trans. Power Electron.*, vol. 14, no. 5, pp. 906–917, 1999.

[8] G. Gohil, L. Bede, R. Teodorescu, T. Kerekes, and F. Blaabjerg, "Line filter design of parallel interleaved vscs for high-power wind energy conversion systems," *IEEE Trans. Power Electron.*, vol. 30, no. 12, pp. 6775–6790, Dec 2015.

[9] G. Gohil, L. Bede, R. Teodorescu, T. Kerekes, and F. Blaabjerg, "Design of the trap filter for the high power converters with parallel interleaved VSCs," in *Proc. 40th Annual Conference on IEEE Industrial Electronics Society, IECON 2014*, Oct 2014, pp. 2030–2036.

[10] Z. Xu, R. Li, H. Zhu, D. Xu, and C. Zhang, "Control of parallel multiple converters for direct-drive permanent-magnet wind power generation systems," *IEEE Trans. Power Electron.*, vol. 27, no. 3, pp. 1259–1270, March 2012.

[11] I. G. Park and S. I. Kim, "Modeling and analysis of multi-interphase transformers for connecting power converters in parallel," in *Proc. 28th Annual IEEE Power Electronics Specialists Conference, 1997. PESC '97 Record.*, vol. 2, 1997, pp. 1164–1170 vol.2.

[12] R. Hausmann and I. Barbi, "Three-phase multilevel bidirectional DC-AC converter using three-phase coupled inductors," in *Proc. IEEE Energy Conversion Congress and Exposition, 2009. ECCE 2009.*, Sept 2009, pp. 2160–2167.

[13] F. Forest, T. Meynard, E. Laboure, V. Costan, E. Sarraute, A. Cuniere, and T. Martire, "Optimization of the supply voltage system in interleaved converters using intercell transformers," *IEEE Trans. Power Electron.*, vol. 22, no. 3, pp. 934–942, 2007.

[14] F. Forest, E. Laboure, T. Meynard, and V. Smet, "Design and comparison of inductors and intercell transformers for filtering of PWM inverter output," *IEEE Trans. Power Electron.*, vol. 24, no. 3, pp. 812–821, 2009.

[15] J. Salmon, J. Ewanchuk, and A. Knight, "PWM inverters using split-wound coupled inductors," *IEEE Trans. Ind. Appl.*, vol. 45, no. 6, pp. 2001–2009, 2009.

[16] B. Cougo, T. Meynard, and G. Gateau, "Parallel Three-Phase Inverters: Optimal PWM Method for Flux Reduction in Intercell Transformers," *IEEE Trans. Power Electron.*, vol. 26, no. 8, pp. 2184–2191, Aug. 2011.

[17] G. Gohil, R. Maheshwari, L. Bede, T. Kerekes, R. Teodorescu, M. Liserre, and F. Blaabjerg, "Modified discontinuous pwm for size reduction of the circulating current filter in parallel interleaved converters," *IEEE Trans. Power Electron.*, vol. 30, no. 7, pp. 3457–3470, July 2015.

[18] G. Gohil, L. Bede, R. Maheshwari, R. Teodorescu, T. Kerekes, and F. Blaabjerg, "Parallel interleaved VSCs: influence of the PWM scheme on the design of the coupled inductor," in *Proc. 40th Annual Conference on IEEE Industrial Electronics Society, IECON 2014*, Oct 2014, pp. 1693–1699.

[19] D. G. Holmes and T. A. Lipo, *Pulse Width Modulation for Power Converters: Principles and Practice*. Hoboken, NJ: Wiley-IEEE Press, 2003.

[20] K. Matsui, Y. Murai, M. Watanabe, M. Kaneko, and F. Ueda, "A pulsewidth-modulated inverter with parallel connected transistors using current-sharing reactors," *IEEE Trans. Power Electron.*, vol. 8, no. 2, pp. 186–191, Apr 1993.

[21] K. Venkatachalam, C. Sullivan, T. Abdallah, and H. Tacca, "Accurate prediction of ferrite core loss with nonsinusoidal waveforms using only steinmetz parameters," in *Computers in Power Electronics, 2002. Proceedings. 2002 IEEE Workshop on*, 2002, pp. 36–41.

[22] J. Li, T. Abdallah, and C. Sullivan, "Improved calculation of core loss with nonsinusoidal waveforms," in *Industry Applications Conference, 2001. Thirty-Sixth IAS Annual Meeting. Conference Record of the 2001 IEEE*, vol. 4, 2001, pp. 2203–2210 vol.4.

[23] P. Dowell, "Effects of eddy currents in transformer windings," *Proceedings of the Institution of Electrical Engineers,*, vol. 113, no. 8, pp. 1387–1394, August 1966.

Ghanshyamsinh Gohil (S'13) received the M.Tech. degree in electrical engineering with specialization in power electronics and power systems from the Indian Institute of Technology-Bombay, Mumbai, India, in 2011.

He is currently working towards the Ph.D. degree at the Department of Energy Technology, Aalborg University, Denmark. Prior to joining the Ph.D. studies, he was employed at Siemens Corporate Technology, Bangalore. His research interests include parallel operation of voltage source converters, pulsewidth modulation techniques and the design of the inductive power components.

Lorand Bede (S'11) was born in Romania in 1989. He received the engineering degree in electrical engineering from Sapientia Hungarian University of Transilvania, Trgu Mure, Romania, 2011, the MSc. degree in Power Electronics and Drives from Aalborg University, Aalborg, Denmark, in 2013. Currently he is a PhD Fellow at the Departmen t of Energy Technology, at Aalborg University, Aalborg. His research interest include grid connected applications based on parallel interleaved converters for wind turbine applications.

Remus Teodorescu (S'94-A'97-M'99-SM'02-F'12) received the Dipl.Ing. degree in electrical engineering from Polytechnical University of Bucharest, Romania in 1989, and PhD. degree in power electronics from University of Galati, Romania, in 1994. In 1998, he joined Aalborg University, Department of Energy Technology, power electronics section where he currently works as full professor. Since 2013 he is a visiting professor at Chalmers University. He has coauthored the book Grid Converters for Photovoltaic and Wind Power Systems, ISBN: 978-0-470-05751-3, Wiley 2011 and over 200 IEEE journals and conference papers. His areas of interests includes: design and control of grid-connected converters for photovoltaic and wind power systems, HVDC/FACTS based on MMC, SiC-based converters, storage systems for utility based on Li-Ion battery technology. He was the coordinator of the Vestas Power Program 2008 2013.

Tamas Kerekes (S'06-M'09) obtained his Electrical Engineer diploma in 2002 from Technical University of Cluj, Romania, with specialization in Electric Drives and Robots. In 2005, he graduated the Master of Science program at Aalborg University, Institute of Energy Technology in the field of Power Electronics and Drives. In Sep. 2009 he obtained the PhD degree from the Institute of Energy Technology, Aalborg University. The topic of the PhD program was: "Analysis and modeling of transformerless PV inverter systems". He is currently employed as an Associate professor and is doing research at the same institute within the field of grid connected renewable applications. His research interest include grid connected applications based on DC-DC, DC-AC single- and three-phase converter topologies focusing also on switching and conduction loss modeling and minimization in case of Si and new wide-bandgap devices.

Frede Blaabjerg (S'86-M'88-SM'97-F'03) was with ABB-Scandia, Randers, Denmark, from 1987 to 1988. From 1988 to 1992, he was a Ph.D. Student with Aalborg University, Aalborg, Denmark. He became an Assistant Professor in 1992, an Associate Professor in 1996, and a Full Professor of power electronics and drives in 1998. His current research interests include power electronics and its applications such as in wind turbines, PV systems, reliability, harmonics and adjustable speed drives. He has received 15 IEEE Prize Paper Awards, the IEEE PELS Distinguished Service Award in 2009, the EPE-PEMC Council Award in 2010, the IEEE William E. Newell Power Electronics Award 2014 and the Villum Kann Rasmussen Research Award 2014. He was an Editor-in-Chief of the IEEE TRANSACTIONS ON POWER ELECTRONICS from 2006 to 2012. He has been Distinguished Lecturer for the IEEE Power Electronics Society from 2005 to 2007 and for the IEEE Industry Applications Society from 2010 to 2011. He is nominated in 2014 by Thomson Reuters to be between the most 250 cited researchers in Engineering in the world.